Materials Characterization 98 (2014) 37–46

Contents lists available at ScienceDirect

Materials Characterization

journal homepage: www.elsevier.com/locate/matchar

High-temperature low cycle fatigue behavior of a gray cast iron

K.L. Fan *[,1], G.Q. He, M. She, X.S. Liu, Q. Lu, Y. Yang, D.D. Tian, Y. Shen

School of Materials Science and Engineering, Tongji University, Shanghai 201804, China

ARTICLE INFO

Article history:
Received 27 May 2014
Received in revised form 11 August 2014
Accepted 6 October 2014
Available online 7 October 2014

Keywords:
Gray cast iron
HT250
High temperature
Low cycle fatigue

ABSTRACT

The strain controlled low cycle fatigue properties of the studied gray cast iron for engine cylinder blocks were investigated. At the same total strain amplitude, the low cycle fatigue life of the studied material at 523 K was higher than that at 423 K. The fatigue behavior of the studied material was characterized as cyclic softening at any given total strain amplitude (0.12%–0.24%), which was attributed to fatigue crack initiation and propagation. Moreover, this material exhibited asymmetric hysteresis loops due to the presence of the graphite lamellas. Transmission electron microscopy analysis suggested that cyclic softening was also caused by the interactions of dislocations at 423 K, such as cell structure in ferrite, whereas cyclic softening was related to subgrain boundaries and dislocation climbing at 523 K. Micro-analysis of specimen fracture appearance was conducted in order to obtain the fracture characteristics and crack paths for different strain amplitudes. It showed that the higher the temperature, the rougher the crack face of the examined gray cast iron at the same total strain amplitude. Additionally, the microcracks were readily blunted during growth inside the pearlite matrix at 423 K, whereas the microcracks could easily pass through pearlite matrix along with deflection at 523 K. The results of fatigue experiments consistently showed that fatigue damage for the studied material at 423 K was lower than that at 523 K under any given total strain amplitude.

1. Introduction

Gray cast iron (GCI) has received extensive attention as a constructional material due to its good castability, corrosion resistance and thermal conductivity, relatively low cost (20–40% less than steel), excellent vibration damping and abrasion resistance [1–3]; this makes GCI more attractive than other types of cast irons and hence widely applied in industry. In particular, it is used in automotive industry like cylinder blocks and heads due to its damping capacity [4] and wear resistance. A key issue regarding automotive applications, such as cylinder blocks, however, is the fatigue performance of the used material. Most previous work on the fatigue of GCI has focused on the application of macroscopic empirical fatigue life correlations [5–7] or on the effects of graphite on fatigue resistance (such as size, morphology and distribution of graphite lamellas) [1,9,10]. It was also reported that the ferritic matrix structure was characterized by cleavage type failure, while a cleavage type failure event happened in the pearlitic matrix structure [11], and other microstructural features, such as the phosphorus content or the size of eutectic cells [1,7], the content of ferrite and pearlite [11], as well as casting defects [12] (i.e. inclusions or porosities), could play a vital role in fatigue behavior of GCI. In addition, studies on the effect of environment [2] and surface treatments [4,13] have provided substantial information on fatigue properties of GCI.

Strain-controlled low cycle fatigue (LCF) can be a primary consideration in the design of products for industrial purposes [14]. Automobile engine cylinders, as is known to all, are frequently subjected to cyclic loading leading to plastic flow, especially under high working temperatures. Thus, strain-controlled LCF is a major cause of damage that, eventually, results in engine material failure at elevated temperatures. However, most previous work [1,6–11,13,15–18] has mainly focused on both stress-controlled high cycle and thermal fatigue behavior in an effort to help design fatigue resistant GCI. Studies on the strain-controlled low cycle fatigue behavior of GCI remain limited to date [19,20]. It was reported by Fash and Socie [19] that cyclic stress–strain response was observed during the tests but the typical stable hysteresis response had not been found. Lee and Lee [20] further observed that tensile–compression asymmetry in the stress–strain response due to the presence of the graphite flakes. However, the influence of the temperature on the strain controlled LCF behavior of GCI is still unknown. For instance, one study has outlined the relationship between temperature and fatigue behavior in stress-controlled high cycle fatigue [21], the fatigue strength remained relatively constant for testing temperatures ranging from 295 K to 523 K, then increased rapidly for temperatures around 623 and 723 K and finally followed by a decrease above 723 K, but such information is not available for strain-controlled LCF condition in GCI. Even worse, this problem has attracted little attentions so far. In this study, by investigating the LCF behavior of HT250 GCI at 423 and

* Corresponding author.
E-mail address: 12klfan@tongji.edu.cn (K.L. Fan).
[1] Postal address: School of Materials Science and Engineering, Tongji University, No. 4800 Caoan Road, Jiading District, Shanghai 201804, China.

http://dx.doi.org/10.1016/j.matchar.2014.10.005
1044-5803/

523 K, the strain controlled LCF mechanism of the HT250 will be studied in depth.

2. Material

The material utilized in this study was a GCI with base composition of C ~ 3.36%, Si ~ 2.06%, Mn ~ 0.71%, Cr ~ 0.23%, S ~ 0.08%, and P ~ 0.02%. Specimens were machined from the boss between commercial automobile engineer cylinder blocks with loading axis along the Z axis direction, as shown in Fig. 1a (marked with red rectangular box). The blocks were made of pearlitic HT250 GCI ("HT" is the abbreviation of "HUI TIE"), which was produced by a gravity casting technology.

3. Experimental procedure

Dog-bone round samples for both tensile and fatigue tests were machined with a parallel gauge section 30 mm long and 6.5 mm in diameter (Fig. 1b). Circumferential machining marks in the gauge length portion of the specimens were mechanically polished by emery papers to minimize machining surface roughness effects on tensile and fatigue. The tensile and LCF tests were performed using an MTS 810 servo-hydraulic test machine (MTS, USA), which was equipped with an induction heating system within the Fangrui Company (China). The temperatures of each sample were monitored by thermocouple and controlled by an induction heating system. The tensile testing was performed at a strain rate of $1 \times 10^{-3}\ s^{-1}$. The LCF tests were carried out at 423 K and 523 K at total strain amplitudes of 0.12%, 0.16%, 0.20% and 0.24%. A symmetrical triangular waveform was used under fully-reversed strain-controlled conditions ($R_\varepsilon = -1$). LCF tests at different strain amplitudes were carried out at a constant strain rate of $0.3 \times 10^{-2}\ s^{-1}$. All tests were started after soaking for 30 min at the test temperatures in order to ensure the uniform temperature throughout the samples. The experiments would be stopped when the stresses dropped about 10%. The metallographic microstructures of the tested alloys were examined using an optical microscope equipped with an image acquisition and analysis system. Fractography and surface relief observations were performed by scanning electron microscopy (SEM). The gauge sections of the specimens were mechanically thinned for the extraction of transmission electron microscopy (TEM) foils. The longitudinal portion of the gauge section was first reduced to approximately 600 μm. The disks thus obtained were mechanically thinned down to approximately 30 μm using carborundum papers. The disks were electropolished using a twin-jet electropolishing with an electrolyte made of 20% $KClO_4$ and 80% CH_3CH_2OH. Microstructural characterization was conducted using a Hitachi H-800 TEM operating at 200 kV.

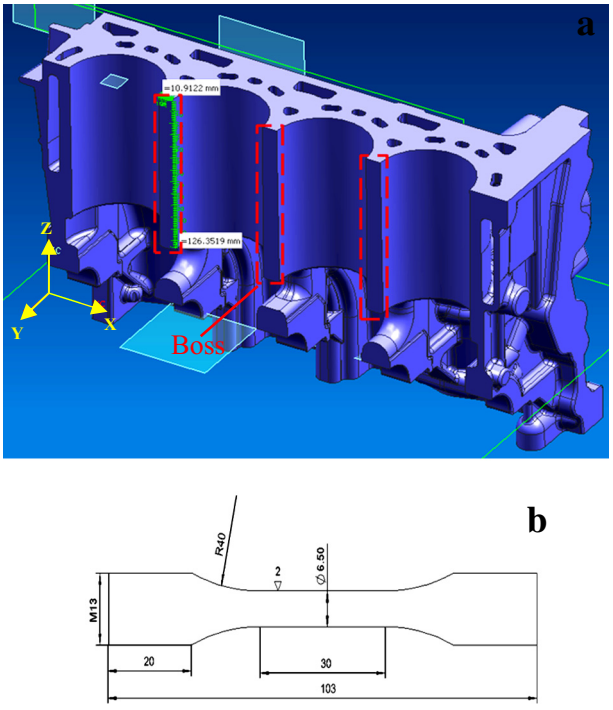

Fig. 1. (a) Location of specimens taken from the automobile engine cylinder block. (b) Sketch of specimen (dimensions in mm). (For interpretation of the references to color in this figure legend, the reader is referred to the web version of this article.)

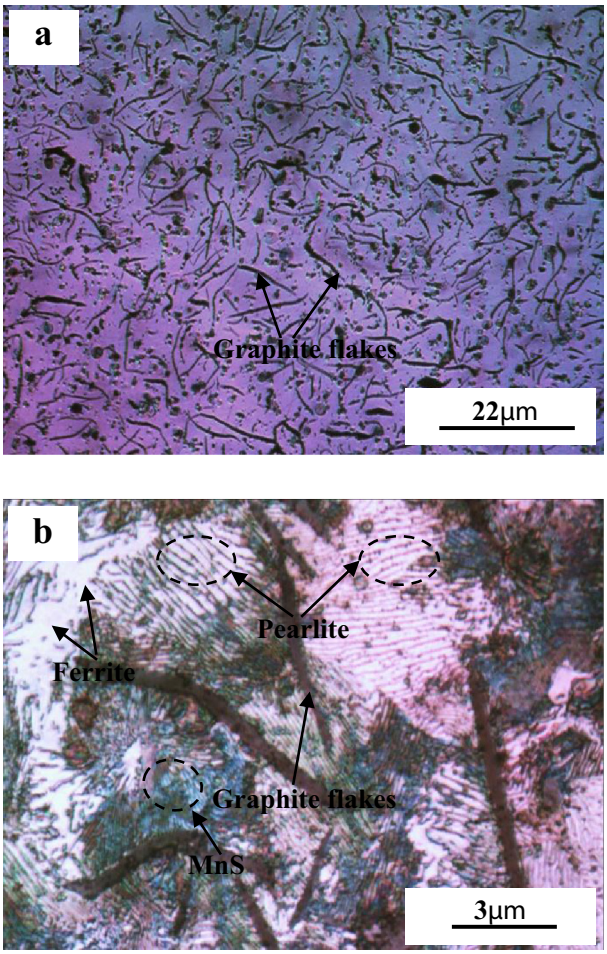

Fig. 2. Typical microstructures of the HT250 sample. (a) Unetched and (b) etched.

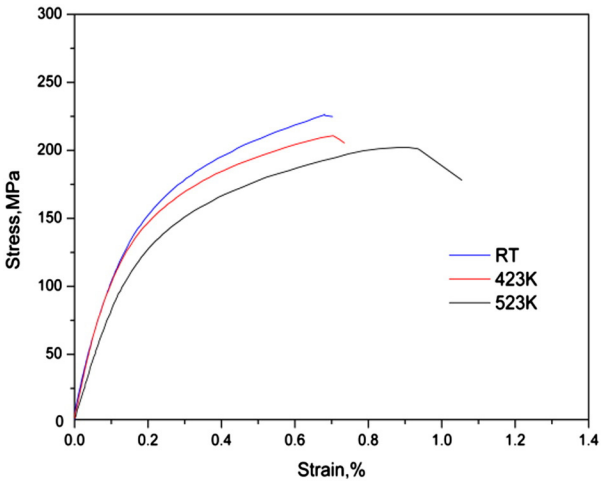

Fig. 3. Tensile stress–strain curves of HT250 GCI at RT, 423 and 523 K.

Table 1
Tensile properties of HT250 GCI at different temperatures.

Temperature	σ_{YS} (MPa)	σ_{UTS} (MPa)	Elongation (%)
RT	190.53	226.18	0.50
423 K	173.68	210.79	0.53
523 K	162.39	202.68	0.89

4. Results

4.1. Microstructural evaluation

The microstructure of the unetched HT250 sample reveals a typical "A type" (ASTM standards [19]), where graphite flakes exist with the matrix, most of which are featured by uniform distribution and random orientation, as shown in Fig. 2a. The mean size of the graphite flakes is approximately 13 μm. Fig. 2b shows the typical microstructure of the etched HT250 sample. The matrix of the pearlitic HT250 is mainly composed of lamellar pearlite (95%) with traces of ferrite (5%). Besides, MnS inclusions (in dark cyan) are present in the microstructure of the sample.

4.2. Tensile properties

The monotonic stress–strain curves for the HT250 at different temperatures are shown in Fig. 3. The detailed mechanical properties are listed in Table 1. As temperature increased, the yield strength (σ_{YS}) and ultimate tensile stress (σ_{UTS}) decreased with the increase of total elongation.

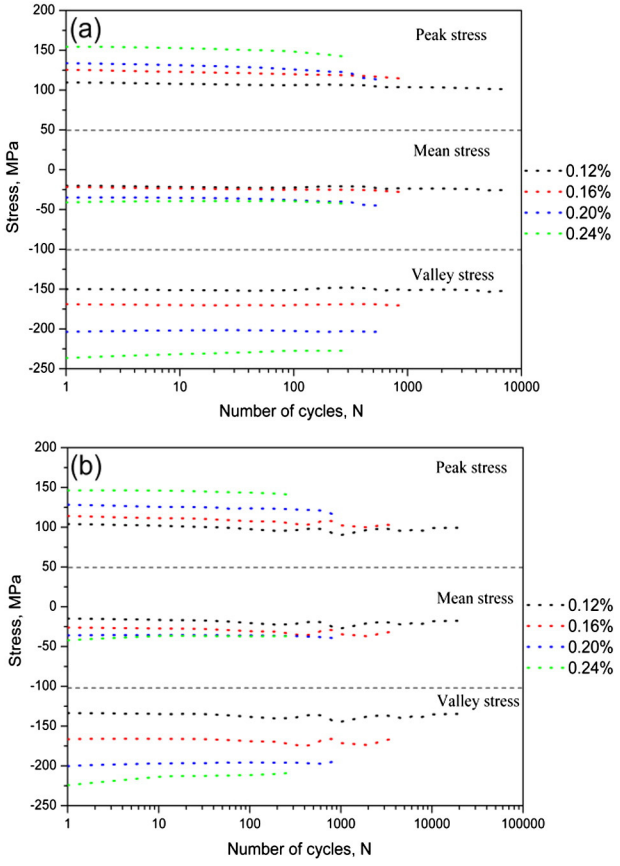

Fig. 4. Stress vs. the number of cycles for HT250 GCI at different temperatures: (a) 423 K and (b) 523 K.

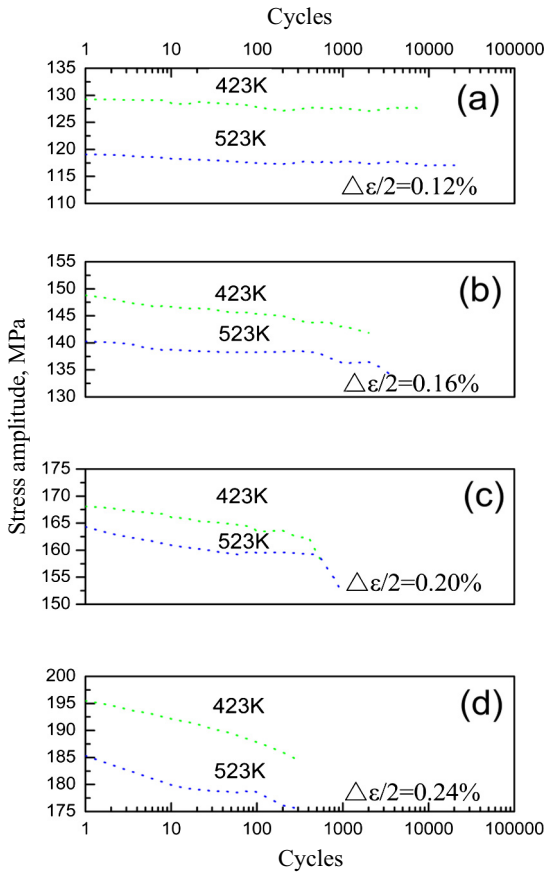

Fig. 5. Stress amplitude vs. the number of cycles for HT250 GCI at different total strain amplitudes. (a) 0.12%, (b) 0.16%, (c) 0.20% and (d) 0.24%.

4.3. Cyclic deformation

Variations of the stress with the number of cycles are shown in Fig. 4. Generally, the peak stress decreased with increasing number of cycles at all total strain amplitudes at 423 and 523 K. This tendency became stronger with the increasing of total strain amplitude. In both cases, however, the evolution of valley stress as a function of the number of cycles was noticeably different at different total strain amplitudes. At a high total strain amplitude of 0.24%, the valley stress progressively increased with increasing loading cycles. For other total strain amplitudes (from 0.12% to 0.20%), the valley stress remained essentially constant as

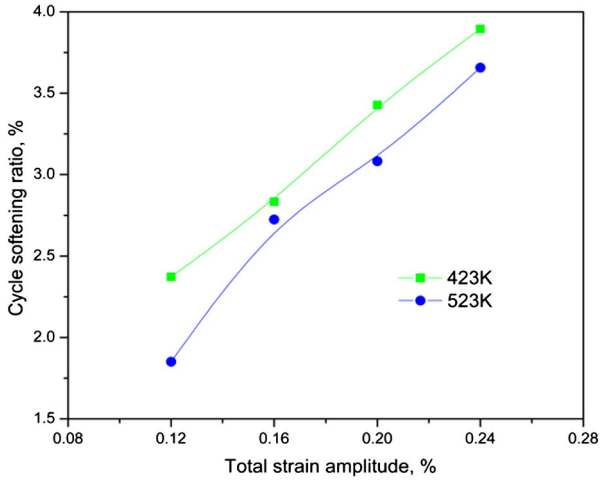

Fig. 6. The cyclic softening ratio *S* computed from cyclic stress response data.

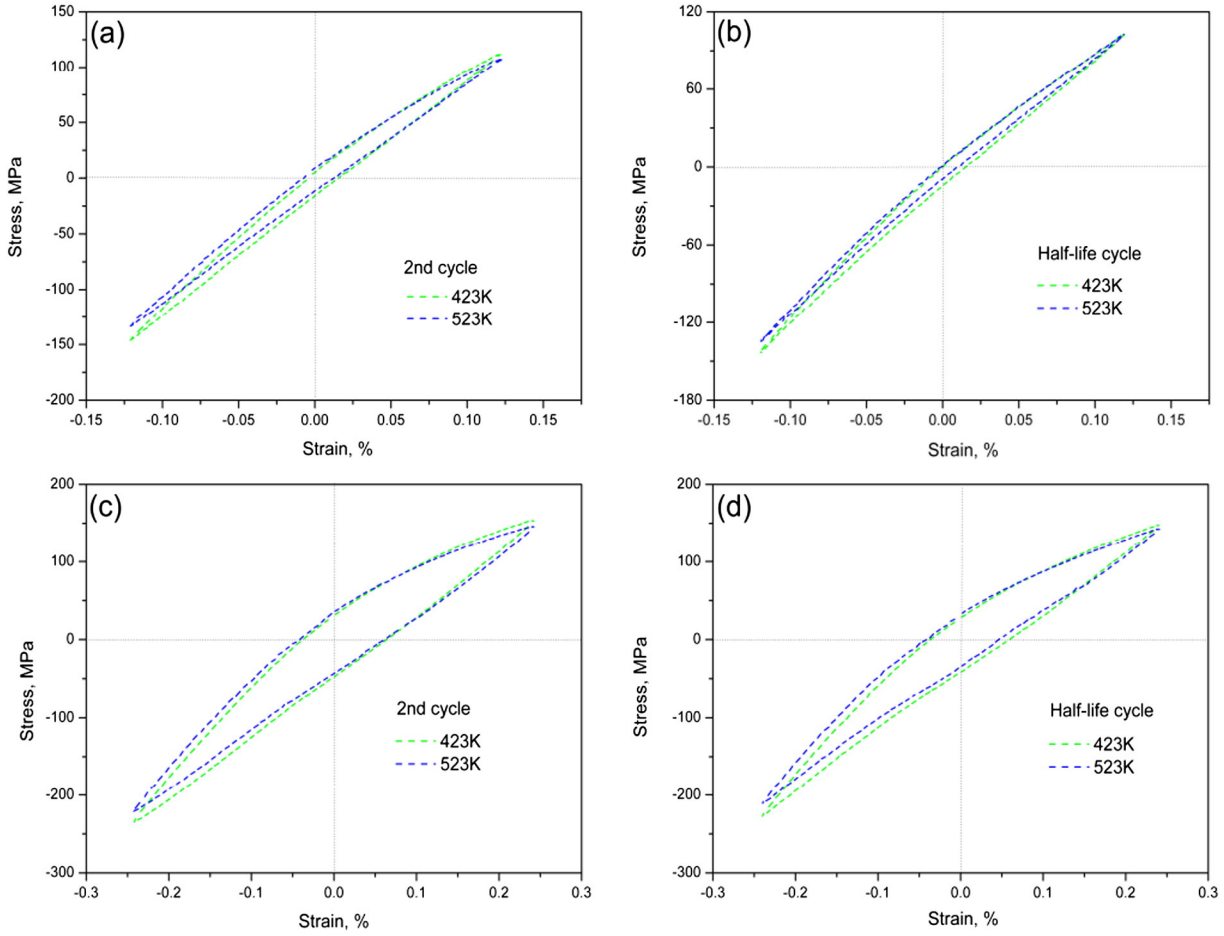

Fig. 7. Stress–strain hysteresis loops of HT250 GCI at different total strain amplitudes: (a) and (b) 0.12%, (c) and (d) 0.24%.

cyclic deformation progressed. Besides, at the low strain amplitudes (0.12% and 0.16%) at 523 K, there existed sudden increase of both the peak stress and valley stress around 600th cycle. Such behavior was probably attributed to the interaction of different load history and environment. Usually, as the total strain amplitude increased, the mean stress decreased at 423 and 523 K. On the other hand, in both cases, the mean stress decreased with increasing cycles to failure at low total strain amplitudes (from 0.12% to 0.20%). Irrespective of the test temperatures, it seemed that mean stress remained nearly constant during cyclic deformation at the total strain amplitude of 0.24%, which was due to the increasing valley stress with increasing loading cycles.

The cyclic stress responses at various strain levels for different test temperatures and $R_\varepsilon = -1$ are shown in Fig. 5. In both cases, the cyclic deformation behavior was noticeably different at any given total strain amplitude. Clearly, the material showed slight softening at the low strain amplitude of 0.12%. By contrast, at higher strain amplitudes (from 0.16% to 0.24%), the tendency of cyclic softening was stronger. Particularly, under any given temperature, the material studied was highly prone to cyclic softening at the high strain amplitude of 0.24%. Besides, under the same total strain amplitude, the cyclic stress amplitudes at 423 K were higher than that at 423 K. In the current study, this could be mainly explained by the tensile strength of the samples (Table 1), where the values of tensile strength at 423 K were higher than that at 523 K.

In order to quantify the softening variation related to an increase of the strain range at 423 and 523 K, the cyclic softening ratio S is computed using the following equation [22]:

$$S(\%) = \left[\frac{(\sigma)/2_{N=1} - (\sigma)/2_{N_{f/2}}}{(\sigma)/2_{N=1}}\right]. \quad (1)$$

Here, $(\sigma)/2_{N=1}$ denotes the stress amplitude for the first cycle and $(\sigma)/2_{N_{f/2}}$ is the stress amplitude at half fatigue life. The corresponding data from the cyclic softening ratio evaluations are summarized in Fig. 6. The variation in S is a function of total strain amplitude $\Delta\varepsilon/2$. Moreover, cyclic softening ratio correlates with temperature.

4.4. Hysteresis loops

Fig. 7 summarizes the typical stress–strain hysteresis loops for the second cycle and mid-life cycle at the selective strain amplitudes

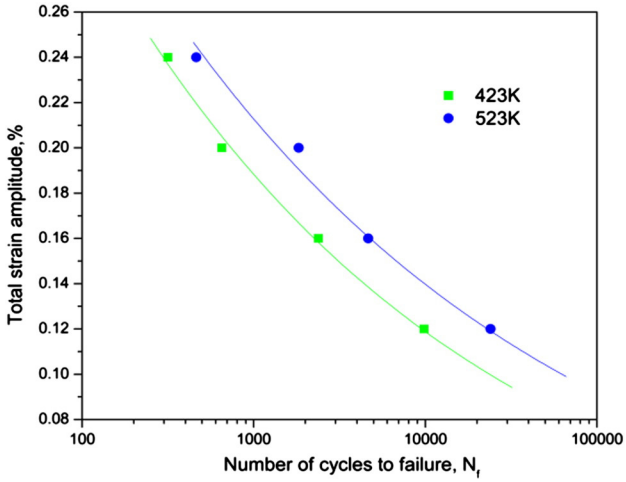

Fig. 8. Dependence of fatigue life on imposed strain amplitude.

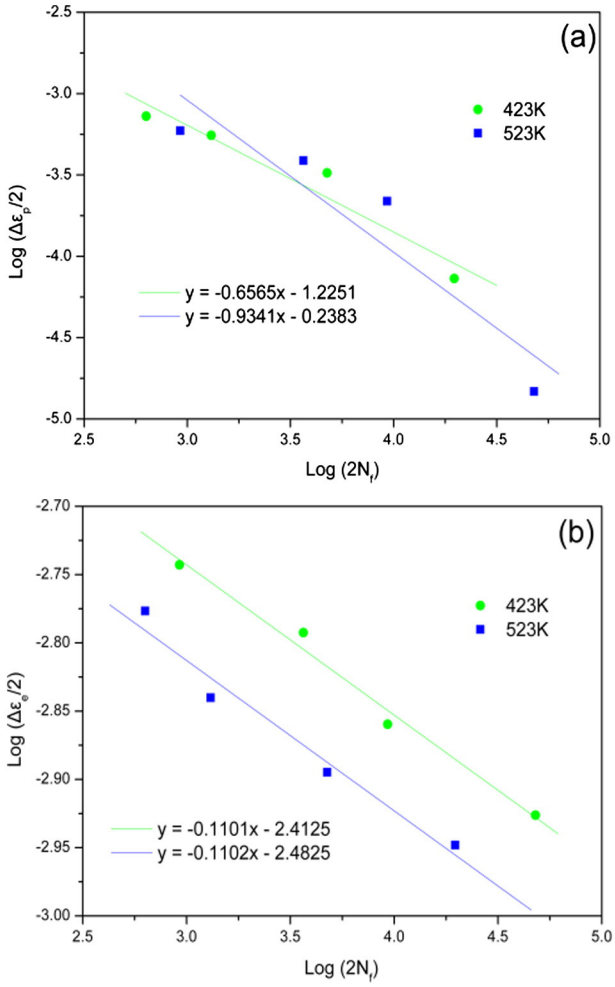

Fig. 9. Evaluation of fatigue parameters for HT250 GCI: (a) Coffin–Manson plot and (b) Basquin plot.

(0.12% and 0.24%). At both the first and mid-life cycle, the hysteresis loops were all asymmetric at 423 and 523 K, where the compression peak was greater than the tension peak. Such phenomenon was also agreed with previous findings on the other GCI [20], where the graphite flakes transmitted the load and their effect on material response was greatly diminished under compressive loads. In both cases, the hysteresis loop at second/half-life cycle became larger in both width and height with increasing total strain amplitude. Under the same total strain amplitude, the compression peak at 523 K was higher than that at 423 K, while the tension peak at 523 K was slightly lower than that at 423 K. This corresponded well to the cyclic deformation characteristics shown in Fig. 4.

4.5. Fatigue life

The fatigue life N_f, obtained as a function of cyclic total strain amplitude $\Delta\varepsilon/2$ at test temperature studied, is plotted in Fig. 8. Obviously, the fatigue life at 523 K is higher than that at 423 K at any given total strain amplitude. The enhanced fatigue life observed also aligned well with the general trend presented in Table 1, showing a higher ductility of the alloy at 523 K, which eventually allow for more tolerance to plastic strain. Moreover, the fatigue life shows a monotonic decrease with increasing total strain amplitude at all test temperatures studied.

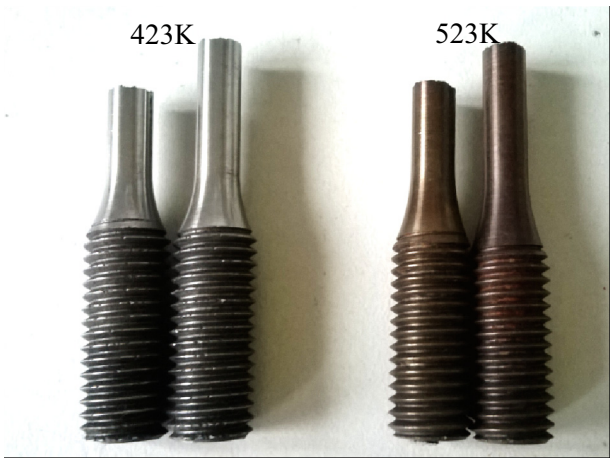

Fig. 10. Surfaces of fractured samples at a total strain amplitude of 0.16% (optical microscope).

Furthermore, the fatigue life can be associated with plastic strain amplitude according to following Coffin–Manson relationship:

$$\frac{\Delta\varepsilon_p}{2} = \varepsilon_f'\left(2N_f\right)^c \tag{2}$$

where ε_f' is the fatigue ductility coefficient, c is the fatigue ductility exponent, N_f is the number of cycles to failure, and $\Delta\varepsilon_p/2$ is the plastic strain range. The $\Delta\varepsilon_p/2$ used in the analysis is acquired at half of the fatigue life ($N_f/2$).

The values of fatigue strength exponent b and fatigue strength coefficient σ_f' could be determined according to the following Basquin's equation,

$$\sigma_a = E\frac{\Delta\varepsilon_e}{2} = \sigma_f'\left(2N_f\right)^b \tag{3}$$

where E is Young's modulus, $\Delta\varepsilon_e$ is the true elastic strain range, and N_f is the number of cycles to failure. These fatigue properties are obtained from regression analysis data, as shown in Fig. 9. The evaluated fatigue parameters in this work are given in Table 2.

4.6. Fractography and fatigue cracks

4.6.1. Main crack initiation and propagation

In the sections that follow, two representative samples loaded at the total strain amplitude of 0.16% at 423 and 523 K were chosen for analysis, and designated as samples S1 and S2, respectively. Examples of macrographs of the fatigue failed samples S1 and S2 are shown in Fig. 10. Compared with sample S1, the surface of sample S2 after failure had a brown color. This implied that significant oxidation occurred in sample S1.

As an example, low-magnification SEM images of main crack initiation site zone of the specimen S1 is presented in Fig. 11a. As indicated, the fatigue crack initiation site in microstructure could not be clearly identified (Fig. 11a). This was similar to fatigue fracture surface features reported for the other GCI [16]. Usually, casting defects such as porosities are especially

Table 2
Fatigue parameters of HT250 GCI at different temperatures.

Temperature	Fatigue ductility exponent, c	Fatigue ductility coefficient, (%)	Fatigue strength coefficient, (MPa)	Fatigue strength exponent, b
423 K	−0.657	0.059	434.656	−0.1101
523 K	−0.934	0.577	325.138	−0.1102

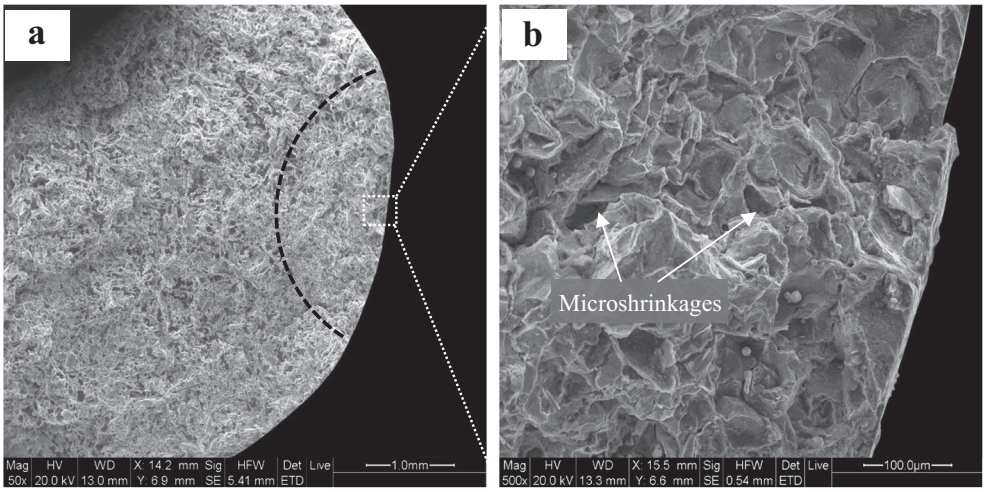

Fig. 11. Typical SEM image of sample S1: (a) the overall view of the fracture surface. Image (b) is the high-magnification observation of the squared area in image (a).

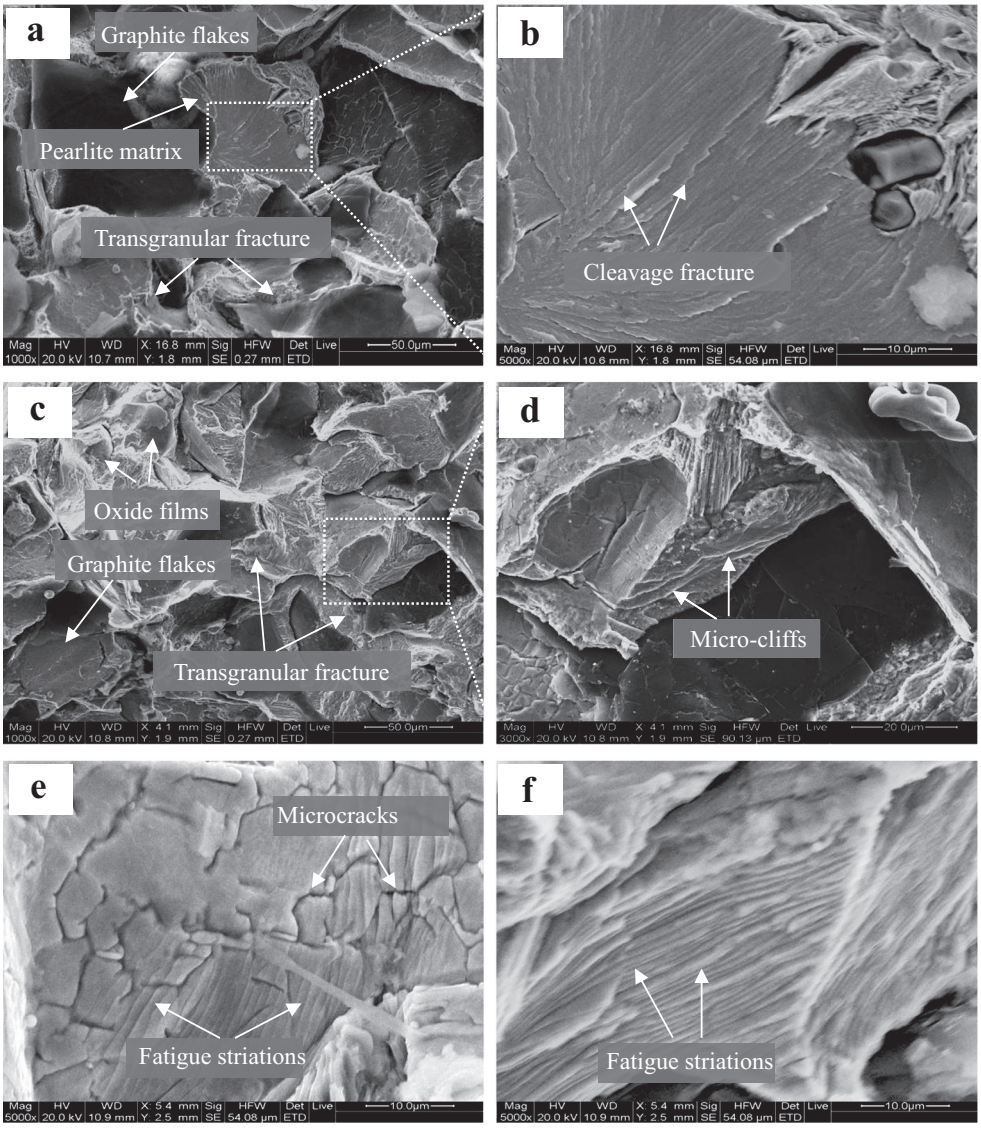

Fig. 12. Fractographs of HT250 GCI showing the main crack propagation area: (a), (b) and (e) sample S1; (c), (d) and (f) sample S2.

harmful to the LCF property of castings due to preferential initiation and propagation of cracks at these sites [23]. Thus, the fatigue cracks probably initiated at these microshrinkages, as shown by higher magnification image in Fig. 11b.

Fig. 12a–f shows the representative SEM images of main crack propagation regions of the tested specimens (S1 and S2) with respect to different temperatures. Fig. 12b and d show the high magnification images of the corresponding squared area in Fig. 12a and c, respectively. Transgranular fracture is predominant at all temperatures studied (Fig. 12a and c), together with some fatigue striations in the ferrite areas (Fig. 12e and f). Besides, some oxide films (Fig. 12c) with microcracks (Fig. 12e) were observed in sample S2. However, it seemed that oxide films were not produced on the fracture faces of sample S1. In the case of sample S2 fatigued, interestingly, some plastic deformation traces could be identified on the facets of micro-cliffs (as indicated by the arrows in Fig. 12d), hinting at a higher ductility of the material at 523 K. For sample S1, however, fan-shaped cleavage facets that had river patterns (Fig. 12a and b), at pearlitic particles, were identified, and implied that the extent of brittle fracture increased as compared with that in sample S2 (Fig. 12c and d). Meanwhile, the cross-sectional areas of the fatigue specimen (S1 and S2) were also photographed by SEM, as shown in Fig. 13a and b. In both cases, it could be seen that main cracks continuously propagated and showed deflection. Additionally, there was a tendency for the formation of microcracks (as marked by white dash circle) occurred at graphite–matrix interfaces/large graphite flakes accompanying the main crack for samples S1 or S2, which could be attributed to the random graphite flake distribution.

4.6.2. Microcrack initiation and propagation

According to Fournier et al. [24], the fatigue life depended largely on the process of crack initiation and propagation to the small crack at elevated temperatures. There was discernable distinction between the microcrack growth patterns at different temperatures for the examined material. Obviously, two microcracks (denoted as "I" and "II") of similar magnitude initiated at sufficiently deformed graphite–matrix interfaces at 423 K (Fig. 14a). Graphite flakes act as stress raisers and induce graphite–matrix interface debonding or self-microcracking during LCF tests. Therefore, microcracks readily initiated at interfaces between the graphite flakes and pearlite matrix in the presence of cycling deformation.

However, the situation changed at 523 K (Fig. 14b). Here we observed, over the whole test specimens (523 K), more microcracks initiation in the larger graphite flakes rather than at the graphite–matrix interfaces. Firstly, this was due to their larger inherent defects than the smaller ones. Secondly, these graphite flakes were often brittle in nature and have a different coefficient of thermal expansion (more pronounced at 523 K) than the pearlite matrix, making them probable locations for crack nucleation. Usually, cleavage of graphite flakes occurs along their basal planes (0001) into a series of distorted hexagons and short sections of prismatic fracture link the islands of cleavage within the flakes [11]. As the deformation proceeded in the wide range of the matrix, these cleaved graphite flakes acted as the sources of microcracks would coalesce into macrocracks and propagate inside the pearlite matrix. Comparing the microstructures for sample S1 (Fig. 14a), however, the microcrack for sample S2 continuously propagated and showed deflection when it traversed pearlite matrix (Fig. 14b).

4.7. TEM observation

TEM investigations are conducted to characterize the development of the dislocation distribution after fatigue (Fig. 15). For samples S1 and S2, dense dislocation arrangements were observed between the

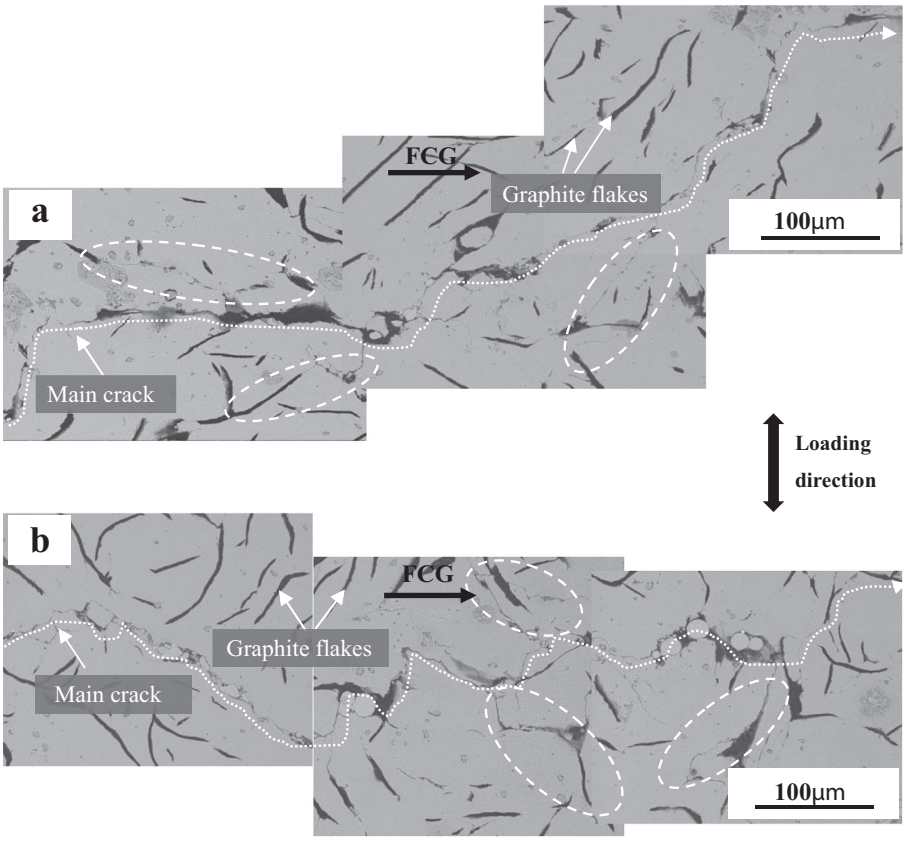

Fig. 13. SEM micrograph associated with main crack propagation path in samples (a) S1 and (b) S2. Note that dark arrows indicate the fatigue crack growth (FCG) direction.

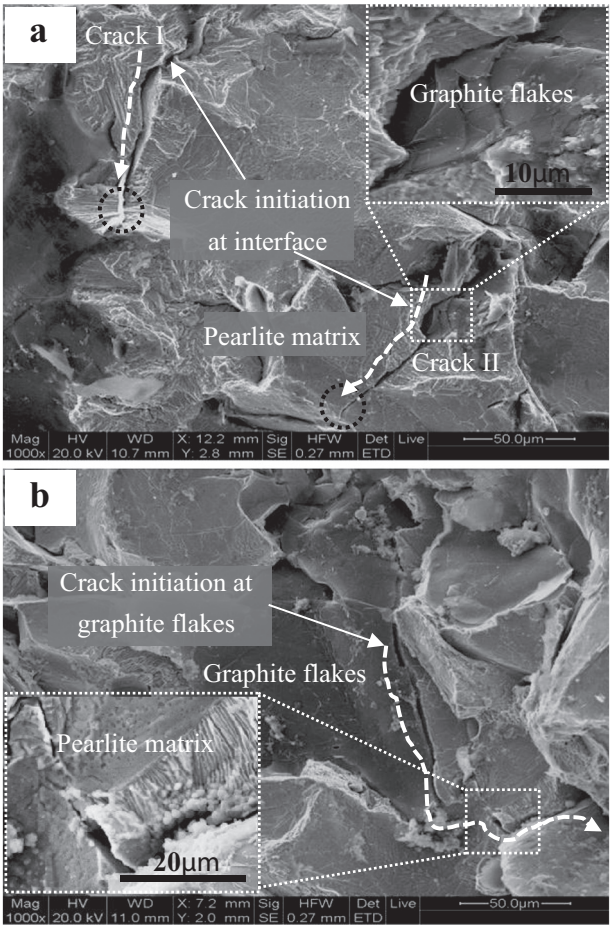

Fig. 14. Fracture surface morphology of the HT250 under LCF in samples (a) S1 and (b) S2, showing the initiation and propagation of the microcracks. The insets are the high-magnification observations of the squared area in image (a) and (b).

cementite lamellae (Fig. 15a and c). This implied that plastic deformation was formed mainly in the ferrite, while cementite lamellae were hardly deformed. For sample S1, there existed regions consisting of dislocation tangles and cells (pointed by white dashed circles) in the ferrite at 423 K, as shown in Fig. 15b. For sample S2, however, the dislocation tangles and dislocation cells might transform into subgrain boundaries, especially where the existence of the cementite in the limited scope is extremely sparse (Fig. 15c). Specifically, one interesting feature in sample S2 is the presence of climb of dislocations, as pointed out by the arrows (Fig. 15d). According to Golanski and Mrozinski [25], elevated temperature can cause an increase in the vacancy density, which helps the dislocation pass round the obstacles (the dislocation climb mechanism).

5. Discussion

5.1. Cyclic deformation characterization

As already seen in Fig. 5, the HT250 GCI showed softening at any total strain amplitudes from 0.12% to 0.20%. Obviously, fatigue cracks continuously propagated and showed deflection (Fig. 13). The fatigue crack initiation and propagation could lead to the bearing section of the sample decreasing and cyclic softening [26]. The TEM observations were also consistent with the cyclic softening behavior observed (Fig. 15a–d). For sample S1, the rearrangement of dislocations into lower-energy configurations in ferrite, such as cell structure (Fig. 15b), is believed to lower the local glide resistance [27], and thus contributes to the cyclic softening phenomenon. On the other hand, the subgrain boundaries for sample S2 led to a decrease in stress amplitude, i.e. cyclic softening (Fig. 15c). For sample S2, interestingly, edge dislocation climbing (Fig. 15d) was more effectively activated under cyclic loading, dislocations moved and annihilated with the opposite sign dislocation, leading to strain softening in the present material as well [28].

5.2. Fatigue life

Analysis of the achieved fatigue graphs (Fig. 8) allows to state that the fatigue life of HT250 GCI depends on the temperature significantly. At high temperatures, the LCF life of the examined material, however, depended on the degree of softening (i.e. the level of cyclic softening ratio S) in the present study (see Fig. 6). Under the same total strain amplitude, the magnitude of S at 523 K was clearly lower than that at 423 K, and the LCF life was drastically improved. It could be presumed, therefore, that the increase in the cyclic softening ratio S due to changes in temperature and total strain amplitude was at least partly responsible for the observed reduction in fatigue life.

However, the decrease in the cyclic softening ratio is not the only factor that makes LCF life improvement at 523 K. Fracture observation (Fig. 12) also indicated that the effects of microstructure on fatigue life of HT250 GCI at test temperatures. Generally, the ductile fracture mechanism is characterized by tearing edges and dimples, whereas the brittle fracture mechanism is normally identified by a relatively featureless fracture surface, such as cleavage facets and river patterns [29]. As already seen from the fracture surface in Fig. 12 b, the sample S1 exhibited some sign of brittle fracture. Indeed, the continuous network of brittle cementite acted as the crack initiation site accentuating the brittle cleavage failure [30], the resulting microstructure led to relatively lower ductility at 423 K. However, one can see that sample S2 was featured by some traits resembling tearing edges on the fracture surface (Fig. 12d). Indeed, in LCF, where crack propagation is dominant, the resistance to fatigue propagation requires ductility [31]. Thus, one factor for the fatigue damage in samples S1 and S2 was associated with the fracture characteristic, which was related to the improvement in the fatigue life of HT250 at 523 K.

As previously mentioned, crack growth period might dominate the fatigue life in LCF. According to Dutta et al. [32], the fatigue crack growth behavior could be influenced by the roughness induced crack closure in this material. Obviously, the fracture surface in fatigue crack propagation regions for the examined sample S1 was flat (see Figs. 12a and 14a), whereas for the sample S2, the fracture surfaces were fairly coarse (Figs. 12c and 14b). Moreover, the nature of the crack propagation was more tortuous in sample S2 compared with that in sample S1 (Fig. 13). It can be seen that, as expected, the higher the temperature, the rougher the crack face as well as more tortuous crack path at the same total strain amplitude. On the other hand, the surface oxidation of sample S2 was remarkable after failure, because of a long term exposure at 523 K (Fig. 10). Additionally, part of the fractured surface for sample S2 was covered by oxidation marks, as compared with sample S1 (Fig. 12). These examinations strongly suggested that the oxidation process significantly involved the fatigue failure process and affected the endurance lifetimes. This was because the formation of the oxide film could also induce crack closure at 523 K, thereby providing crack growth retardation [31,33]. In general, each fatigue striation normally represents a single cycle [34]. Under the same total strain amplitude, the striation distance for sample S1 was wider than that of sample S2 (see Fig. 12e and f), which meant, the fatigue crack resistance was smaller and the fatigue crack could expand easily for the former. Thus, the higher fatigue crack propagation resistance for sample S2 would be produced by crack tip shielding due to crack deflection, roughness-induced and oxide-induced crack closure. In such case, this suggested a strong tendency for fatigue damage related to lower testing temperature.

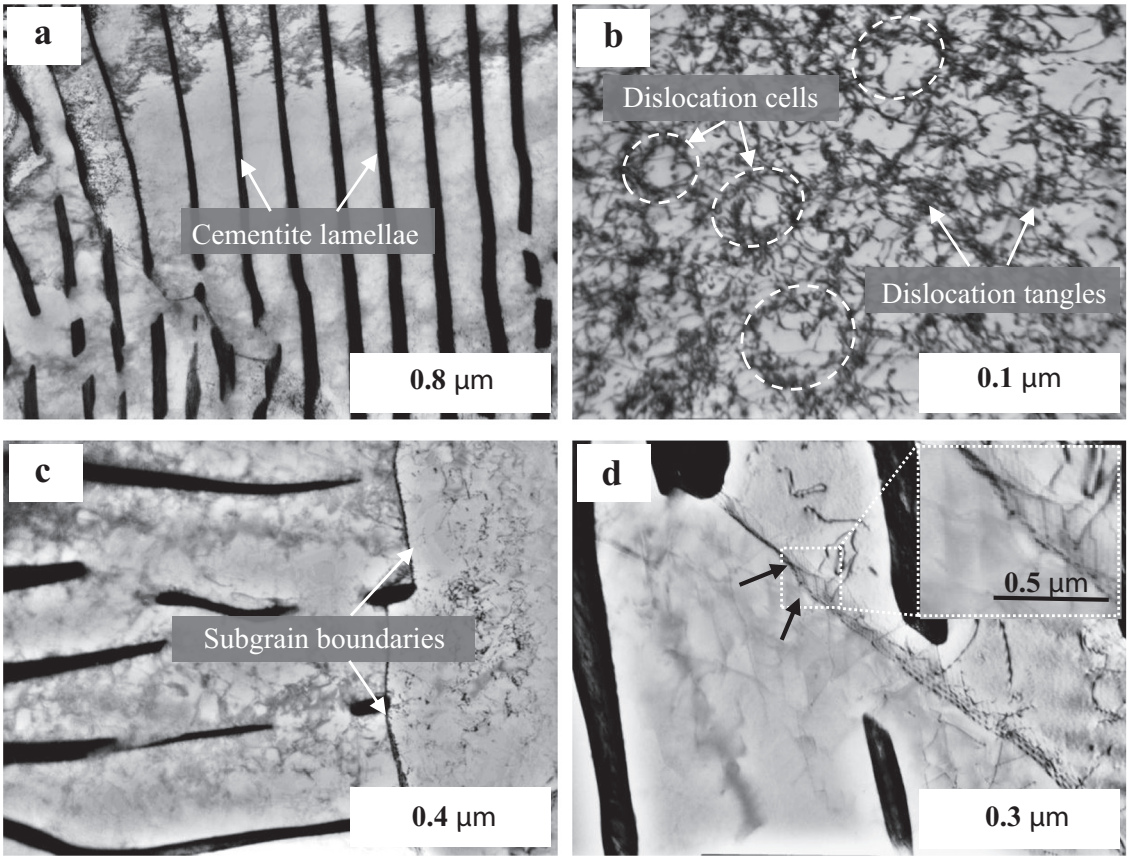

Fig. 15. The dislocation substructure with the total strain amplitude of 0.16%: (a) and (b) sample S1; (c) and (d) sample S2.

In order to understand the reason behind the increase in fatigue life at the same strain amplitude at 523 K, the nature of the stresses generated on pearlite during micro crack propagation is also considered in our study. According to Glover and Pollard [35], the propagation of brittle cracks in pearlite seemed more difficult and cracks were often observed to terminate in or at the boundary of pearlite region. Thus, the fatigue crack could only propagate a short distance before meeting obstacles in the form of other pearlite lamellae [35], in this case, possibly because of the hard pearlite phase acting as a crack arrester. This clearly indicated that fatigue crack propagation in the matrix could be effectively retarded by the pearlite phase. Therefore, stronger stress concentrations ahead of fatigue crack tip could easily occur in the matrix during strain holding. As an example, at the total strain amplitude (0.16%), microcracks were readily blunted during growth inside the pearlite matrix at 423 K (see Fig. 14a). However, the microcrack could easily pass through pearlite matrix combined with deflection at 523 K (Fig. 14b). Likewise, as mentioned earlier, the HT250 showed a higher ductility at 523 K (compared with that at 423 K). It was also plausible to postulate that the effect on microcracks growth was related to the different degree of plasticity ahead of the crack tip at different temperatures. Thus, at the same total strain amplitude, it was possible that the degree of plasticity ahead of the crack tip increased with increasing temperature, resulting in a relatively easy crack propagation and deflection at 523 K. Consequently, at a given strain amplitude, the degree of stress concentrations ahead of crack tip at 423 K was higher than that at 523 K, meaning a lower intensity of fatigue damage and a higher fatigue life at 523 K. However, the effect of plasticity by temperature and/or total strain amplitude on the propagation rates of microcracks cannot be discussed quantitatively on the basis of the current study, and detailed experimental and modeling studies are required to clarify this important point.

6. Conclusions

LCF studies on HT250 GCI for commercial automobile engine cylinder blocks at 423 and 523 K under fully reversed ($R_\varepsilon = -1$) constant total strain amplitude cycling revealed the following:

(1) The material showed slight softening at a lower strain amplitude of 0.12%. By contrast, at higher strain amplitudes (from 0.16% to 0.24%), the tendency of cyclic softening became stronger. Moreover, this material exhibited asymmetric hysteresis loops due to the presence of the graphite lamellas. The cyclic softening characterization was mainly attributed to main fatigue crack initiation and propagation. The TEM observations were also in accordance with the cyclic softening behavior observed. Dislocation cell structure during cyclic deformation was observed at 423 K. However, the developed subgrain boundaries and dislocation climbing were the main dislocation structure at 523 K.

(2) Under the same total strain amplitude, the fatigue life of the examined HT250 at 423 K was higher than that at 523 K. Additionally, the fatigue life showed a monotonic decrease with increasing total strain amplitude at test temperatures.

(3) The surface of sample at 523 K after failure had a brown color. Moreover, the fatigue crack initiation site in microstructure could not be clearly identified. The transgranular fracture was predominant in main crack propagation regions for all samples S1 and S2. For sample S1, microcracks initiated at sufficiently deformed graphite–matrix interfaces. For sample S2, however, more microcracks initiated in the larger graphite flakes rather than at the graphite–matrix interfaces.

(4) Owing to lower plasticity and higher cyclic softening ratio, the HT250 GCI showed a higher fatigue life at 523 K (compared with

that at 423 K) at any given stain amplitude. Moreover, the fatigue life of the HT250 would be also affected by fracture surface roughness, oxidation phenomenon, as well as stress concentrations ahead of crack tip.

Acknowledgments

The authors would like to thank Mr. Z.Y. Xu and Mr. L.Q. Wang for the sample preparation and fatigue tests.

References

[1] L. Collini, G. Nicoletto, R. Konecna, Microstructure and mechanical properties of pearlitic gray cast iron, Mater. Sci. Eng. A 488 (2008) 529–539.
[2] M.N. James, L. Wenfong, Fatigue crack growth in austempered ductile and grey cast irons—stress ratio effects in air and mine water, Mater. Sci. Eng. A 265 (1999) 129–139.
[3] D. Holmgren, I.L. Svensson, Thermal conductivity–structure relationships in grey cast iron, Int. J. Cast Met. Res. 18 (2005) 321–330.
[4] S.H. Choo, S. Lee, S.J. Kwon, Surface hardening of a gray cast iron used for a diesel engine cylinder block using high-energy electron beam irradiation, Metall. Mater. Trans. A 30 (1999) 1211–1221.
[5] D. Taylor, J. Li, A. Giese, Short fatigue crack growth in cast iron described using P-a curves, Int. J. Fatigue 3 (1995) 201–206.
[6] D. Taylor, M. Hughest, D. Allen, Notch fatigue behaviour in cast irons explained using a fracture mechanics approach, Int. J. Fatigue 18 (1996) 439–445.
[7] A.N. Damir, A. Elkhatib, G. Nassef, Prediction of fatigue life using modal analysis for grey and ductile cast iron, Int. J. Fatigue 29 (2007) 499–507.
[8] P. Baicchi, L. Collini, E. Riva, A methodology for the fatigue design of notched castings in gray cast iron, Eng. Fract. Mech. 74 (2007) 539–548.
[9] D.D. Goettsch, J.A. Dantzig, Modeling microstructure development in gray cast irons, Metall. Mater. Trans. A 25A (1994) 1063–1079.
[10] E. Hornbogen, Fracture toughness and fatigue crack growth of grey cast irons, J. Mater. Sci. 20 (1985) 3897–3905.
[11] J.H. Bulloch, Near-threshold fatigue behavior of flake graphite cast irons microstructers, Theor. Appl. Fract. Mech. 24 (1995) 65–78.
[12] D.J. Weinacht, D.F. Socie, Fatigue damage accumulation in grey cast iron, Int. J. Fatigue 9 (1987) 79–86.
[13] X. Tong, H. Zhou, L.Q. Ren, Z.H. Zhang, R.D. Cui, W. Zhang, Thermal fatigue characteristics of gray cast iron with non-smooth surface treated by laser alloying of Cr powder, Surf. Coat. Technol. 202 (2008) 2527–2534.
[14] ASTM E 606–04, Standard Practice for Strain-controlled Fatigue Testing, ASTM International, West Conshohocken, PA, United States, 2012. 636.
[15] H. Mohebbi, D.A. Jesson, M.J. Mulheron, P.A. Smith, The fracture and fatigue properties of cast irons used for trunk mains in the water industry, Mater. Sci. Eng. A 527 (2010) 5915–5923.
[16] S. Kawaguchi, R. Hamanaka, T. Tagawa, The effect of mean stress on the fatigue strength of gray cast iron was examined and its mechanism was investigated, J. Jpn. Inst. Metals 98 (2012) 442–449.
[17] X. Tong, H. Zhou, Z.H. Zhang, N. Sun, H.Y. Shan, L.Q. Ren, Effects of surface shape on thermal fatigue resistance of biomimetic non-smooth cast iron, Mater. Sci. Eng. A 467 (2007) 97–103.
[18] S. Ghodrat, T.C. Riemslag, L.I. Kestens, M. Janssen, J. Sietsma, Effects of holding time on thermomechanical fatigue properties of compacted graphite iron through tests with notched specimens, Metall. Mater. Trans. A 44A (2012) 2121–2130.
[19] J. Fash, D.F. Socie, Fatigue behaviour and mean effects in grey cast iron, Int. J. Fatigue 4 (1982) 137–142.
[20] K.O. Lee, S.B. Lee, Definition of damage parameter in low-cycle fatigue of gray cast iron, Key Eng. Mater. 345–6 (2007) 367–370.
[21] ASM Handbook: Properties and Selection: Irons, Steels, and High-performance Alloys, 10th ed. ASM International — The Materials Information Society, Materials Park, Ohio, 1990. (vol. 1).
[22] H.W. Hoppel, Z.M. Zhou, H.R. Mughrabi, Z. Valiev, Microstructural study of the parameters governing coarsening and cyclic softening in fatigued ultrafine-grained copper, Philos. Mag. A 82 (2002) 1781–1794.
[23] H. Mayer, M. Papakyriacou, B. Zettl, S.E. Stanzl-Tschegg, Influence of porosity on the fatigue limit of die cast magnesium and aluminium alloys, Int. J. Fatigue 25 (2003) 245–256.
[24] D. Fournier, A. Pineau, Low cycle fatigue behavior of Inconel 718 at 298 K and 823 K, Metall. Trans. A 8 (1977) 1095–1105.
[25] G. Golanski, S. Mrozinski, Low cycle fatigue and cyclic softening behaviour of martensitic cast steel, Eng. Fail. Anal. 35 (2013) 692–702.
[26] S.M. Yin, S.X. Li, Low-cycle fatigue behaviors of an As-extruded Mg–12%Gd–3%Y–0.5%Zr alloy, J. Mater. Sci. Technol. 29 (8) (2013) 775–780.
[27] M.C. Carroll, L.J. Carrloll, Developing dislocation subgrain structures and cyclic softening during high-temperature creep–fatigue of a nickel alloy, Metall. Mater. Trans. A 44A (2013) 3592–3607.
[28] H.W. Zhou, Y.Z. He, M. Cui, Y.W. Cen, J.Q. Jiang, Dependence of dynamic strain ageing on strain amplitudes during the low-cycle fatigue of TP347H austenitic stainless steel at 550 °C, Int. J. Fatigue 56 (2013) 1–7.
[29] A. Saha, D.K. Mondal, K. Biswas, J. Maity, Development of high strength ductile hypereutectoid steel by cyclic heat treatment process, Mater. Sci. Eng. A 541 (2012) 204–215.
[30] ASM International Handbook Committee, ASM Handbook, Fractography, vol. 12, ASM International, Materials Park, OH, 1987.
[31] S. Suresh, Fatigue of Materials, 2nd ed. Cambridge University Press, 1998.
[32] V.B. Dutta, S. Suresh, R.O. Ritchie, Fatigue crack propagation in dual phase steels: effects of ferrite–martensite microstructures on crack path morphology, Mater. Trans. A 15A (1984) 1193–1207.
[33] Z.H. Zhong, Y.F. Gu, T. Osada, Y. Yuan, C.Y. Cui, T. Yokokawa, T. Tetsui, H. Harada, Fatigue crack growth characteristics of a new Ni–Co-base superalloy TMW-$_4$M$_3$: effects of temperature and load ratio, J. Mater. Sci. 46 (2011) 7573–7581.
[34] G.E. Dieter, Mechanical Metallurgy, 3rd ed. McGraw-Hill, New York, 1986.
[35] A.G. Glover, G. Pollard, The brittle fracture of gray cast iron, JISI 120 (1971) 138–141.